PCCP

Accepted Manuscript

ROYAL SOCIETY OF CHEMISTRY

www.rsc.org/pccp

ARTICLE TYPE www. rsc.org/xxxxxx | XXXXXXXX

First-principles study of ground-state properties of U_2Mo†

Xin Wang,[a,b] Xiyue Cheng,[b] Yuting Zhang,[a] Ronghan Li,[b] Weiwei Xing,[b] Pengcheng Zhang*[a] and Xing-Qiu Chen[b‡]

Received Xth XXXXXXXXXX 20XX, Accepted Xth XXXXXXXXX 20XX
First published on the web Xth XXXXXXXXXX 200X
DOI: 10.1039/b000000x

By means of first-principles calculations, we have systematically investigated the structural, elastic, vibrational, thermal and electronic properties of the ground-state phase for the intermetallic compound U_2Mo. Our results uncover that the previously synthesized *I*4/*mmm* structure of U_2Mo is a metastable phase and unstable, neither thermodynamically nor vibrationally at the ground state. In combination with the evolutionary structural searches, our first-principles calculations suggest a new ground-state *Pmmn* phase, which has been theoretically confirmed to be stable, both thermodynamically and vibrationally. Moreover, through the DFT+D technique we have discussed the van der Waals interactions on the structural, elastic and vibrational properties, revealing a weak effect in pure U and Mo solids and U_2Mo alloy. The analysis of the electronic band structures evidences its electronic stabilities with the appearance of a deep valley of the density of states at the Fermi level. Moreover, we have further investigated the temperature-dependent structural, thermal expansion and elastic properties of our proposed *Pmmn* ground-state phase. These results are expected to stimulate further experimental investigations of the ground-state phase of U_2Mo.

1 Introduction

In comparison with the mixed-oxide (MOX) fuels, the metallic fuels exhibit significant potential advantages for fast reactors due to its superior properties. It has been applied for a rather long history[1]. For instance, the first prototype fast breeder reactor, Clementine, became operational in 1949 at the Los Alamos National Laboratory using metallic fuel (*i.e.*, δ-stablized plutonium). The main concern of the metallic nuclear fuels is its irradiation performance and compatibility with cladding materials. However, the early metallic fuels (*i.e.*, Pu-Fe and Pu-Al alloys) often suffered from high swelling rates and high smearing density. In the mid-1980s, fuels with U-Zr and U-Pu-Zr alloys showed a significantly better performance and were able to be operated at higher temperatures and higher burn-up. In the 1990s, a variety of U-Pu-*X* ternary alloys (*X* = Mo, Nb, Ti and Zr) have been tested as fuels for fast reactors in the USA and Europe with various degrees of success. In recent years, the developments of TRU-burning advanced fast nuclear reactors (the abbreviation TRU states for so-called transuranium) and accelerator driven system (ADS) call for new concept of fuel types because those reactors share two different considerations, simultaneously: waste incineration and power generation. For them, U-based metallic fuels become promising candidates due to their high heavy metal densities and excellent thermal conductivities.

Within this context, extensive studies on metallic fuels have been performed[2–10]. Among them, U-Mo alloys have been thought to be the most prominent candidates because of their more stable irradiation performance compared with other high density uranium alloys and compounds (*e.g.*, U_3Si, U_6Fe and U_6Mn[11]). Interestingly, Mo has a high solubility (*ca. 35at.%*) in γ-U at high temperature above 833 K. However, below this temperature, the Mo-soluted γ-U alloy is decomposed into α-U and U_2Mo. The experimental measurement already revealed that U_2Mo crystallizes in the $C11_b$ ($MoSi_2$ prototype with the space group of *I*4/*mmm*) structure. To date, there have been experimental investigations on the thermodynamic properties for various U-Mo alloys[9,12,13]. In particular, for U_2Mo some thermodynamic properties have been measured[14]. Recently, using Mo doping combined with ultrafast cooling, Tkach *et al.*[15] have investigated the fundamental electronic properties including Sommerfeld coefficient, magnetic susceptibility of γ-U. Their results have uncovered that the Mo-doped γ-U exhibits a conventional BCS superconductivity with T_c *ca.* 2.1 K and a critical field exceeding 5 T for the 15 at%Mo-soluted alloy. Moreover, no magnetic properties have been observed for U_2Mo, indicating a possible paramagnetic state.

In fact, during the past few decades, many theoretical and computational results on U-based alloys have been published,

† Electronic Supplementary Information (ESI) available: See DOI: 10.1039/b000000x/

[a] *Science and Technology on Surface Physics and Chemistry Laboratory, Mianyang, Sichuan, China.*
[b] *Shenyang National Laboratory for Materials Science, Institute of Metal Research, Shenyang, Liaoning, China.*
Corresponding authors:
‡ Xingqiu Chen xingqiu.chen@imr.ac.cn;
∗ Pengcheng Zhang E-mail: zpc113@sohu.com;

despite of several crucial challenges on U and its alloy. One of the most crucial aspects is that the light-actinide metals, from Th to Pu, pose a severe challenge to modern electronic-structure theory partially due to the existence of highly directional and localized f-electron bonding states. Moreover, the heavy nuclei of the light-actinide metals induce a large relativistic effect on their valence-band structures, and usually require inclusion of the spin-orbit coupling (SOC) effects. Despite of those challenges, some basic properties (such as, zero-pressure zero-temperature equilibrium volumes and bulk modulus) can be successfully derived for the light-actinide metals[16] using all-electron, full-potential, electronic-structure method: the full-potential linear augmented-plane-wave (FLAPW) and the linear combinations of Gaussian-type orbitals-fitting function (LCGTO-FF) methods. It has been recognized that for the ground-state orthorhombic α-U phase, the equilibrium and structural properties[17], elastic constants[18], phonon spectra[19], various defects[20–22], and even subtle electronic-structure details related to charge-density waves[23] have been all well described within conventional DFT[24]. However, for strongly correlated uranium dioxide[25,26] and uranium mononitride[27], the DFT+U treatment has been applied to reproduce well the experimental findings. Some investigations also demonstrated that the standard DFT methods are validate in describing the point defect properties of UC[28,29] and UN[30].

As yet there has only been few attempts to perform *ab initio* study of the formation enthalpy of Mo-soluted γ-U alloys. Through the cluster expansion technique[31] within the Ising Hamiltonian formalism with a set of effective cluster interactions defined by the direct inversion method from the total energies of 16 bcc-based ordered structures, U_2Mo was found to be stable because of its negative formation enthalpy. However, the temperature of phase equilibria transferred into a disordered phase was estimated to be excessively high, *ca.* 2273 K for U_2Mo, which is much higher than the experimental value of *ca.* 853 K[14]. Using the exact muffin-tin orbital method (EMTO) and full-potential linear muffin-tin orbital method (FPLMTO), Landa *et al.*[32] have calculated the formation energy and electronic density of states (DOS) for the disordered Mo-soluted γ-U alloy in comparison with the ordered U_2Mo. The results showed a significant reduction of the DOS in the vicinity of the Fermi level(E_F) in the case of the ordered phase, which causes a decrease of the band-structure contribution to the total energy. Recently, S.Jaroszewicz *et al.*[33] have derived the thermal properties of the U_2Mo by full-potential LPAW method.

Here, through first-principles calculations within the framework of standard density functional theory (DFT), DFT+D and hybrid functional (HSE) by including the nonlocal exchange-interaction effect, we have calculated the thermodynamic, mechanical, elastic and vibrational properties of U_2Mo. Our results demonstrated that the previously characterized tetragonal $C11_b$ phase of U_2Mo is unstable, neither energetically nor vibrationally. Alternatively, utilizing the evolutionary search of USPEX[34–36] we have found a new ground-state phase of U_2Mo, which crystallizes in the orthorhombic structure (*Pmmn*). The derived phonon and elastic properties confirmed its dynamical and mechanical stability. It has also been found that the inclusion of the van der Waals interactions within the DFT+D method does not alter those properties. In addition, we have analyzed its thermodynamical properties including thermal-expansion and specific heat properties as compared with the available experimental results. The paper is organized as follows. Pertinent details of the computational methods are described in section **2**. Results and discussions of the density-functional calculations of the ground-state properties are provided in section **3**. Lastly, concluding remarks are presented in Section **4**.

2 Computational Method

We have employed the Vienna *ab initio* Simulation Package (VASP)[37–39] by utilizing the projector augmented wave (PAW) method[40,41] within the framework of density functional theory (DFT)[42,43]. The description of the exchange-correlation adopted the Perdew, Burke and Ernzerho (PBE)[44] generalized gradient approximation (GGA). The $\vec{k}$-space integration with the incompletely filled orbitals has been performed with the tetrahedron method[45] with Blöchl correction method[46]. Optimizations are achieved by minimizing forces and total energies. The convergence criterion of the total energy and the force were set to be 0.01 meV and 0.001 eV/Å, respectively. The semicore $6s^26p^65f^36d^17s^2$ of U and the valence state $4d^55s^1$ of Mo have been included in the PAW potentials. We used a plane wave cut-off energy of 400 eV, which has been found to be sufficient for precise energetics for all the elements considered in present work. For the calculations of elastic constants, the elastic tensor is determined by performing finite distortions of the lattice and deriving the elastic constants from the strain-stress relationship[47]. The elastic tensor is calculated both, for rigid ions, as well as allowing for internal relaxation of the ionic Hessian matrix and multiplying with the internal strain tensor[48]. The final elastic moduli including both, the contribution of distortions with rigid ions and the contributions from the ionic relaxations, are presented. In order to compute polycrystalline elastic moduli, the Voigt-Reuss-Hill approximation[49–51] are applied. The polycrystalline mechanical properties calculated here include shear modulus (G), Young's modulus (E), Poisson's ratio (ν), and the Debye temperature (Θ_D)[18]. For the bulk properties of the tetragonal and orthorhombic U_2Mo, the $7\times7\times7$ and $13\times13\times15$ k-mesh sampling has been applied, respectively, in the Brillouin Zone (BZ) according to the Monkhorst-Pack

scheme[52]. During our calculations, the spin-polarized calculation has been considered, but U_2Mo is indeed nonmagnetic. Therefore, the nonspin-polarized calculation were adopted for all the calculations. To determine the ground-state enthalpy of formation, we have also calculated the total energies of bcc U and Mo metals with the 19×19×19 *k*-mesh sampling and 500eV cut off energy.

It is well-known that U often exhibits the localized *f*-electronic states we have hence introduced the hybrid functional (HSE)[53,54] to calculate the total energies and electronic structure of U_2Mo. The HSE employs an admixture of Hartree-Fock-like nonlocal exchange interaction and Perdew-Burke-Ernzerhof (PBE) exchange in the construction of the many-body exchange(x) and correlation (c) functional as follows,

$$E_{xc}^{HSE} = \frac{1}{4}E_x^{HF,sr,\mu} + \frac{3}{4}E_x^{PBE,sr,\mu} + E_x^{PBE,lr,\mu} + E_c^{PBE}, \quad (1)$$

where (sr) and (lr) refer to the short- and long-range parts of the respective exchange interactions whereas μ controls the range separation of the Coulomb kernel, varying between 0.2 and 0.3 $Å^{-1}$. We have used $\mu = 0.2$ $Å^{-1}$. The HSE functional is largely self-interaction free thus improving over the standard DFT description and enables us to achieve a correct understanding of strongly correlated electronic systems[55–59]. In the case of HSE06 calculations, a 5×5×5 and 4×3×7 *k*-mesh sampling have been used for *I*4/*mmm* and *Pmmn* phases of U_2Mo, respectively, and a 9×9×9 *k*-mesh sampling for *bcc* phases of U and Mo.

It has recently been recognized that the van der Waals interactions are necessary for accurately calculating bulk moduli and vibrational corrections in some solids[60]. Therefore the DFT+D method[61–63] has also been applied to the present cases and the role of the van der Waals interactions on the structural, elastic and vibrational properties has been discussed. In the case of DFT+D calculations, the parameters were obtained by using the dftd3[62,63] program, and the rest parameters (*i.e.*, cut off energy, *k*-mesh sampling) for the structure relaxation, elastic, vibrational properties are set as the same as standard DFT. The obtained results are listed in Table 1, along with available experimental data.

The phonon spectra and thermodynamic properties have been derived within the code of Phonopy[64,65] by constructing the supercell approach within the conventional DFT framework. Real-space force constants of supercell was calculated by Parlinski-Li-Kawazoe method[66] with a finite displacement (FD) method of 0.01 Å, and the phonon frequencies are calculated from the force constants. The 2×2×2 supercell are chosen to calculate thermodynamic properties using quasiharmonic approximations (QHA) at seven volumes.

3 Results and discussions

3.1 Structural stabilities and enthalpies of formation of U_2Mo

We have first performed a structural search for the ground-state phase of U_2Mo by USPEX in conjunction with VASP codes within the standard DFT framework. Interestingly, the USPEX search has found that the most stable ground-state phase is the orthorhombic *Pmmn* structure for U_2Mo,

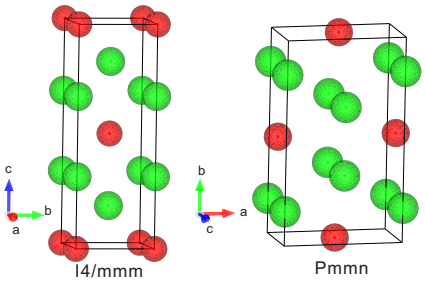

Fig. 1 (color online) The structures of U_2Mo (Left panel: *I*4/*mmm* and right panel: *Pmmn*). The red and green circles are Mo and U atoms, respectively.

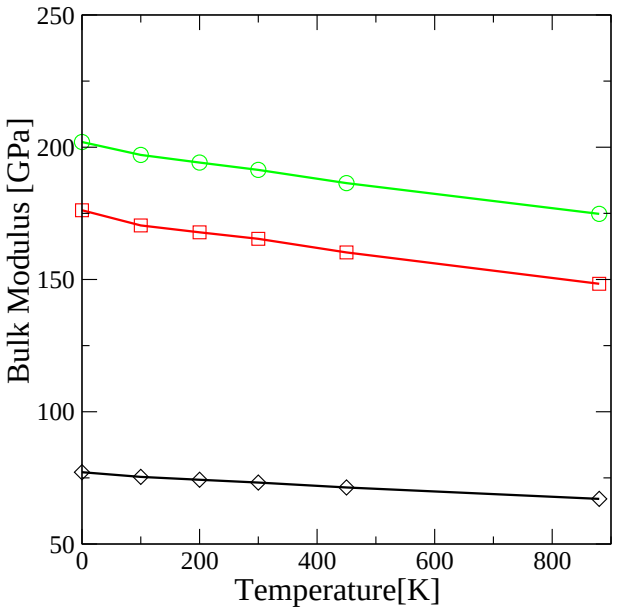

Fig. 2 (Color online) Bulk modulus of *Pmmn* U_2Mo as a function of temperature within standard DFT. The Black, red and green lines denote the shear modulus, bulk modulus and elastic modulus, respectively.

as shown in Fig. 1 (right panel). In contrast, the experimentally synthesized *I*4/*mmm* phase (in Fig. 1(left panel)) is not the energetically lowest one. Structurally, the proposed ground state *Pmmn* phase is indeed closely related with the metastable *I*4/*mmm* phase. As illustrated in Fig. 1, the structural distortion of the *I*4/*mmm* phase by elongating the *a* axis but shortening both the *c*- and *b*-axes, the *Pmmn* structure will appear. The optimized lattice parameters (lattice constants and atomic positions) are complied in Table 1 and the relaxed structural parameters of the *I*4/*mmm* phase derived by standard DFT calculations with the PBE functional are in nice agreement with available experimental findings[67]. However, the DFT+D schemes underestimate the lattice parameters of $Im\bar{3}m$-U, $Im\bar{3}m$-Mo and *I*4/*mmm*-U_2Mo, compared with the experimental findings[67–69].

In addition, their enthalpies of formation have been calculated according to the expression[70] as follows,

$$\Delta H_f = \frac{E_{total}^{U_2Mo} - [2E_{solid}^{U} + 1E_{solid}^{Mo}]}{3} \quad (2)$$

where $E_{total}^{U_2Mo}$ is the total energy of the U_2Mo at the equilibrium state, and E_{solid}^{U} and E_{solid}^{Mo} are the energies of *bcc* U and Mo, respectively. The obtained findings are listed in Table 1. As yet there has been no experimental enthalpy of formation reported for U_2Mo. Our calculated results within standard DFT-PBE calculations demonstrated that the *Pmmn* phase has an enthalpy of -0.145 eV/atom, which is more stable by about 0.042 eV/atom than that of the *I*4/*mmm* phase. Our calculated enthalpy of -0.103 eV/atom for the *I*4/*mmm* phase is lower than the earlier theoretical data of -0.064 eV/atom and -0.034 eV/atom calculated by the cluster expansion in combination of FLAPW method[31] and the EMTO-FPLMTO method[32], respectively. Through the HSE calculations, the proposed *Pmmn* phase is still more stable by about 0.11 eV/atom than the *I*4/*mmm* phase, further evidencing that the *Pmmn* phase is the ground-state phase. Furthermore, the HSE-derived enthalpies of formation of both *Pmmn* and *I*4/*mmm* phases are -0.144 eV/atom and -0.037 eV/atom, respectively. For the former the HSE-derived value is nearly the same as what the DFT-PBE derives, whereas for the latter the HSE-derived value is only about one third of the DFT-PBE data. It also needs to mention that the HSE-derived enthalpy of formation of the *I*4/*mmm* phase almost equals to the value obtained using EMTO-FPLMTO method[32], as shown in Table 1. The DFT+D derived enthalpies of formation of both *Pmmn* and *I*4/*mmm* phases are -0.161 eV/atom and -0.090 eV/atom, respectively; they suggest that the *Pmmn* phase is the ground-state one.

3.2 Temperature-dependent elastic properties from 0 K to 880 K

We have further calculated the elastic constants of the single crystalline *I*4/*mmm* and *Pmmn* phases of U_2Mo in Table 2. We noted that the elastic constants of the *I*4/*mmm* phase was also calculated by Jaroszewicz *et al.*[33]. Except for C_{66}, all other elastic constants are in good agreement to each other between our current data and the previous calculations. Interestingly, the C_{66} value is about 20 GPa, which is very soft[33]. However, using the same method of the Blöch correction (BC) as what Jaroszewicz *et al.* adopted, we have obtained a negative C_{66} of -12 GPa, as shown in Table 2. In particular, it has been noted that because the C_{66} itself is too small its value is very sensitive to the choice of how the partial occupation is set for each orbital during the calculations. If the Methfessel-Paxton method[71] (MP) is used for the partial occupancies with the small enough smearing-parameter, the C_{66} and C_{44} values are both small (9 GPa and 8 GPa, respectively). This fact demonstrated that the crystal of the *I*4/*mmm* phase is very soft/unstable against the shear deformation along the directions of the C_{66} or C_{44} elastic tensors. Moreover, the DFT+D scheme overestimates the elastic constants but does not change the instability of *I*4/*mmm* phase, as shown in Table 2. Furthermore, we have also computed the elastic constants of the *Pmmn* phase in Table 2, evidencing that both BC and MP methods yield very consistent data. In addition, those elastic constants derived both by standard DFT and DFT+D schemes for the *Pmmn* phase satisfy the mechanical stability criteria[72] of the orthorhombic system: $C_{11} > 0, C_{22} > 0, C_{33} > 0, C_{44} > 0, C_{55} > 0, C_{66} > 0, C_{11}+C_{22}+C_{33}+2(C_{12}+C_{13}+C_{23}) > 0, C_{11}+C_{22}-2C_{12} > 0, C_{11}+C_{33}-2C_{13} > 0$, and $C_{22}+C_{33}-2C_{23} > 0$. These facts demonstrate the elastic stability of the *Pmmn* phase. Based on the derived elastic constants, we further calculated their Young's modulus, Shear modulus, Possion's ratio, sound speed (transverse sound speed, V_t, longitudinal sound speed, V_l, average sound speed, V_m), and Debye temperature, as shown in Table 2. The Debye temperature(Θ_D) is known as an important fundamental parameter closely related to many physical properties such as specific heat and melting temperature. The Θ_D shows that, above this temperature, all the long-range acoustic modes will become active, but below it only a part of them can be evoked. The Θ_D is 265 K for *Pmmn*, being higher than the Θ_D of 195 K for *I*4/*mmm*. Moreover, the Θ_D for *Pmmn*, decreases from 265 K to 249 K with temperature increasing from 0 K to 880 K, as shown in Table 3. In addition, we have also derived the temperature-dependent shear modulus, isothermal bulk modulus and elastic modulus of the *Pmmn* phase of U_2Mo in Fig. 2, as well as the temperature-dependent elastic constants, as shown in Table 3. It can been seen that with increasing temperature the three moduli and elastic constants decrease slowly.

3.3 Vibrational properties

We further calculated the phonon dispersions for both *I*4/*mmm* and *Pmmn* phases of U_2Mo. Figure 3 compiled the derived phonon dispersions and the phonon densities of states of both *I*4/*mmm* and *Pmmn* phases of U_2Mo using the 3×3×3 and 2×2×2 supercells, respectively. For the *I*4/*mmm* phase, it can been seen that, around the high-symmetry P-N direction, the two acoustical phonon branches exhibit highly large imaginary frequencies, in particular, being close to the boundary of the BZ. This fact indicates that this *I*4/*mmm* structure is dynamically unstable, agreeing well with the above analysis of the elastic constants. The DFT+D scheme derived phonon dispersions of both *I*4/*mmm* and *Pmmn* phases do not significantly change (see Supplementary Fig. S1†). These results reveal that the van der Waals interactions on pure U solid and its alloy is very weak. The detailed analysis demonstrates that the structural instability easily occurs by the deformation in the *ab* plane, as indicated by the imaginary frequency branches along the high-symmetry N-P direction and the negative elastic constant (C_{66}). For instance, we adopted the strain deformation along the diagonal direction of the *ab* plane of the *I*4/*mmm* phase via the strain tensor as follows,

$$\begin{pmatrix} 1.0 & \frac{1}{2}\sigma & 0 \\ \frac{1}{2}\sigma & 1.0 & 0 \\ 0 & 0 & 1.0 \end{pmatrix} \quad (3)$$

where σ is the strain applied to the *a* and *b* axes. The deformation energies are compiled as a function of σ in Fig. 4. It can be seen that, with increasing σ from zero to around 8%, the deformation energies reduces dramatically. This fact directly reveals the structural instability of the *I*4/*mmm* phase. Furthermore, for the energy-lowest *Pmmn* phase the phonon dispersions shown in Fig. 3 shows no any imaginary frequencies, suggesting its dynamical stabilities. Because the atomic masses of Mo and U are highly different, the phonon densities of states can be clearly separated by Mo and U. As shown in Fig. 3, the low-frequency region (below 4 THz) is dominated by the U atom because the acoustical models are mainly originated from the heavy elements and above 5 THz it is obvious that the phonon modes are mainly from the Mo atoms. Finally, according to the phonon densities of states the zero-point vibrational energies for both *I*4/*mmm* and *Pmmn* phases can be derived to be 0.054 and 0.066 eV/f.u., respectively. It needs to be emphasized that the zero-point vibrational energy may not be accurate because of the existence of the imaginary frequencies.

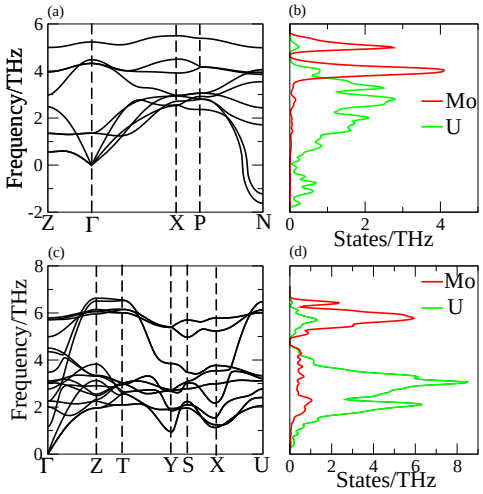

Fig. 3 (color online) (a) The phonon spectrum of *I*4/*mmm* (b) The phonon density of states of *I*4/*mmm* (c) The phonon spectrum of *Pmmn* (d) The phonon density of states of *Pmmn*.

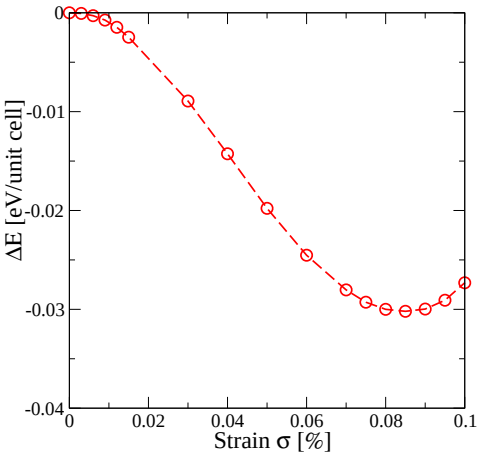

Fig. 4 (color online) The deformation energies derived from DFT-PBE calculations as a function of the strain, σ, as applied in Equation (3). With σ=0, the undeformed structure is the *I*4/*mmm* one.

3.4 Thermal volume expansion and specific heat of U_2Mo

As the metallic fuel, one would concern seriously the thermodynamic properties, in particular, the thermal expansion of volumes and the specific heats. In order to elucidate these properties, we have calculated the DFT static energies $U(V)$ and the phonon free energies $F_{\text{phonon}}(T;V)$ at seven different volumes around the the equilibrium state[65]. The thermodynamic functions $G(T,p) = \min_V[U(V) + F_{\text{phonon}}(T;V)$ were fitted to the integral form of the Vinet equation[73] of state (EOS) at the pressure of p = 0. The Gibbs free energies at finite

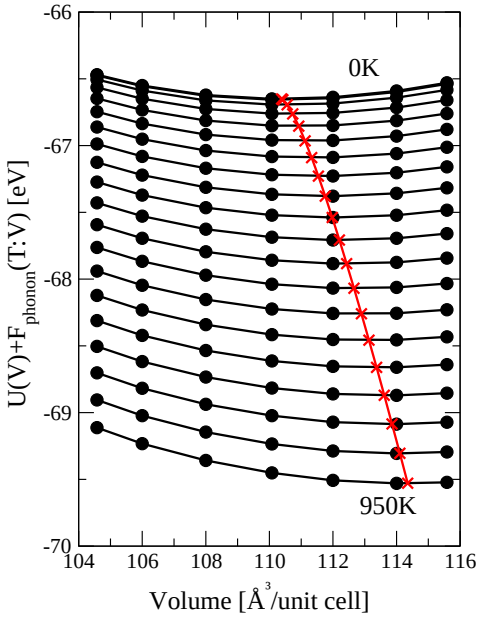

Fig. 5 (color online) $U(V)+F_{phonon}(T;V)$ as a function of unit cell volume of the *Pmmn* phase of U_2Mo. The circles denote $U(V)+F_{phonon}(T;V)$ calculated at the volume points at every 50 K between 0 and 950 K. The solid curves show the fitted thermodynamic functions. The minimum values of the fitted thermodynamic function of temperatures are depicted by the crosses. The red curve passing through the crosses is guide to the eye.

temperatures were obtained at the minimum values of the thermodynamic functions, the corresponding equilibrium volumes and the isothermal bulk moduli were obtained also from the Vinet EOS. The corresponding results of the *Pmmn* phase of U_2Mo are compiled in Fig. 5. It can be seen that the thermal expansion of the volume is observed with the increasing equilibrium volume. Therefore, based on these data, we have derived the thermal volume expansion (including thermal expansion coefficients) of the ground-state *Pmmn* phase of U_2Mo. It needs to be emphasized that, because the *I*4/*mmm* phase at its equilibrium state exhibits negative phonon modes, hence there is no way to calculate its thermal expansion properties. As illustrated in Fig. 6 of the *Pmmn* phase, the thermal volume expansion, which was defined as $\Delta L/L_0$ (L_0 is $L=V^{1/3}$ at 300 K and $\Delta L = L - L_0$), is compiled as a function of temperatures. It can be seen that the thermal expansion of the volumes increase as the temperature increases. Surprisingly, above 400 K the theoretically derived values of the *Pmmn* phase agree well with the experimentally measured data of the *I*4/*mmm* phase. It has been noted that U_2Mo exhibits a high-temperature disordered $\gamma(U,Mo)$ transformation above 853 K[14]. But, in our

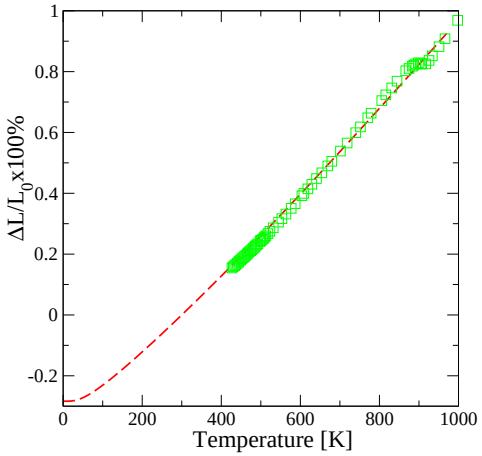

Fig. 6 (color online) The volume expansion of *Pmmn* U_2Mo as a function of temperature within standard DFT. The red dashed curve denotes the calculated values of *Pmmm* U_2Mo and the experimental values of *I*4/*mmm* U_2Mo are depicted by the green squares (Ref[14])

current calculations no disordered transition has been considered. The thermal expansion coefficients of the *Pmmn* phase of U_2Mo have been further compiled in Fig. 7.

Furthermore, the heat capacities C_p at the constant pressure calculated by *QHA* and C_v at the constant volume of *Pmmn* U_2Mo have been derived as shown in Fig. 7, as well as the

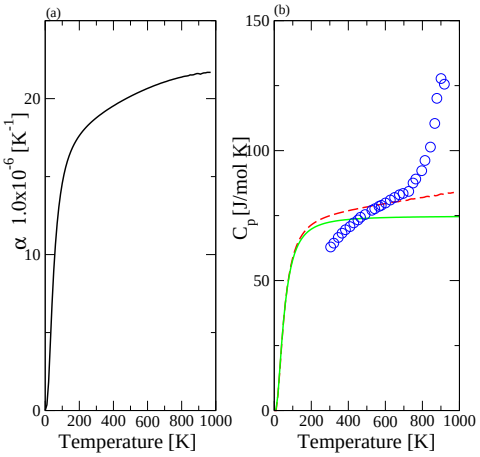

Fig. 7 (color online)(a) Thermal expansion coefficients of *Pmmn* U_2Mo as a function of temperature within standard DFT. (b) Heat capacities of U_2Mo as a function of temperature. The red dashed and green solid curves denote the calculated values of C_p(QHA) and C_v(HA) for *Pmmn*, respectively. The experimental values of *I*4/*mmm* U_2Mo are depicted by the blue circles(Ref[14]).

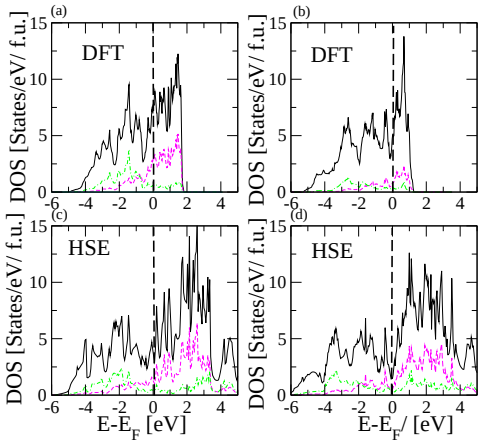

Fig. 8 (color online) The calculated densities of states (DOSs) of the *I*4/*mmm* (panels: a and c) and the *Pmmn* phases (panels: b and d) with the standard DFT (panels: a and b) and the HSE (panels: c and d) frameworks. The black curves denote the total DOSs. The U-5*f* and Mo-4*d* projected local DOSs depicted by magenta dashed and green dashed dot curves, respectively.

experimental data of *I*4/*mmm* phase[14]. As temperature increases, it grows rapidly up to *ca.* 150 K but a nearly constant at high temperatures above *ca.* 200 K. The discrepancies between C_p and C_v of the *Pmmn* phase is very small at low temperature. This fact can be interpreted by the following well-known thermodynamic relationship between C_p and C_v,

$$C_p = C_v + BVT\alpha^2, \quad (4)$$

where α is the coefficient of volumetric thermal expansion while B is the bulk modulus. Based on a purely harmonic model, there is no thermal expansion and C_v must be equal to C_p. The term $BVT\alpha^2$ can thus be viewed as the correction arising from the anharmonic effect. However, it has been noted that the C_p of the *Pmmn* phase of U_2Mo agrees well with the experimental data of the *I*4/*mmm* phase in the temperature range from 400 K to 750 K. The experimental peak of the C_p curve above about 800 K corresponds to the ordered to disordered transformation of U_2Mo. In our calculations, currently there is no way to consider this.

3.5 Electronic structure

To elaborate the electronic properties, we have further calculated the electronic densities of states (DOSs) for both the *I*4/*mmm* and *Pmmn* phases of U_2Mo within standard DFT and HSE framework at their equilibrium volumes (Fig. 8). The most typical feature of their DOSs is that the density at the Fermi level significantly alters from the *I*4/*mmm* to the *Pmmn* phases. Within the standard DFT-PBE framework the Fermi level lies at a sharp peak showing a highly high density for the *I*4/*mmm* phase, whereas for the *Pmmn* phase a significant decrease of the density is evidenced because the Fermi level now occupies the nearly pseudogap in the case of *Pmmn* phase. Moreover, for *I*4/*mmm*, the Mo-4*d* electrons exhibit very low densities above the Fermi level, and thus would not be expected to play a major role in bonding, whereas for *Pmmn*, Mo-4*d* and U-5*f* electrons show a relatively stronger hybridization. Around the Fermi level that is mainly dominated by the *f* orbital, the *f* occupation exhibits significant variance upon these two structures, as shown in Figs. 8(a) and (b). It can be seen that the density of states at the Fermi level, N(E_F) = 5 states eV^{-1} f.u^{-1}, for the *Pmmn* phase shows a significant decrease, as compared with the N(E_F) of 7.5 states eV^{-1} f.u.$^{-1}$ for the *I*4/*mmm* phase. This fact reveals the electronic stability of *Pmmn* phase, in agreement with the comparisons of the total energies, elastic constants and phonon spectra. Importantly, this large change becomes more apparent within the HSE framework due to the fact that the nonlocal exchange interaction heavily separates the Mo-*d* and U-*f* states around the Fermi level. As illustrated in Fig. 8(d) the Fermi level now lies in the deep valley, with a density of only about 1.5 states eV^{-1} f.u.$^{-1}$, which is only 30% of the DFT-PBE derived density, as shown in Fig. 8(b). In particular, the consistent fact for both DFT-PBE and HSE-derived DOSs is that, when comparing with the *I*4/*mmm* phase, the decrease of the density at the Fermi level for the *Pmmn* phase is mainly due to the separations of the occupied bonding and unoccupied antibonding states, implying the electronic stability in the *Pmmn* phase.

4 Conclusions

In summary, we have systematically explored the ground-state properties of U_2Mo from first-principles calculations. In combination with the evolutionary structural searches, we have proposed a new ground-state *Pmmn* phase, which is theoretically confirmed to be stable within standard DFT, HSE and DFT+D framework. The *Pmmn* ground-state phase is indeed closely correlated with the previously characterized *I*4/*mmm* phase. As comparison with available experimental data of the *I*4/*mmm* phase, the standard DFT calculations accurately yielded the lattice constants. The DFT calculation underestimates the enthalpy of formation when comparing with the early reported FP-LMTO results for which an agreement has been, however, achieved by the HSE calculations. However, the addition of dispersion corrections destroys the perfect agreement of lattice parameters of $Im\bar{3}m$-U and $Im\bar{3}m$-Mo with experimental achieved at the DFT level. The elastic and vibrational properties of *I*4/*mmm* and *Pmmn* phases have been derived within the standard DFT and DFT+D framework. The detailed analysis demonstrated that the mechanical insta-

bility of *I*4/*mmm* stems from the deformation in the *ab* plane, whereas the ground-state *Pmmn* phase is both dynamically and thermodynamically stable, without any imaginary frequencies in its phonon dispersions. The DFT+D method increases the elastic constants but does not change the mechanical and vibrational instabilities of *I*4/*mmm*. These results reveal that the van der Waals interactions is very weak in pure U and Mo solids and U_2Mo alloys. The analyses of the derived DOSs demonstrated the electronic instability of the *I*4/*mmm* as compared with the *Pmmn*: the total electronic density at the Fermi level of *Pmmn* is significantly reduced with respect to that of *I*4/*mmm*. Finally, we have derived the temperature-dependent structural, elastic, and thermal expansion of volume as well as specific heats of U_2Mo at its ground state. We hope that these theoretical results will further stimulate the experimental investigation of the ground-state properties of U_2Mo.

Acknowledgments

This work is supported by NSFC under the grants No.91226203, 91226204 and 51174188. The authors also acknowledge the computing resources from Supercomputing Center (including its Shenyang Branch in IMR) of Chinese Academy of Science (CAS) and the local HPC cluster of the Materials Process Modeling Division in the IMR as well as the National Supercomputing Center in Tianjin (TH-1A system).

References

1 S. S. Hecker and M. Stan, *J. Nucl. Mater.*, 2008, **383**, 112–118.
2 D. Keiser Jr and M. Dayananda, *J. Nucl. Mater.*, 1993, **200**, 229–243.
3 T. Ogata, M. Kurata, K. Nakamura, A. Itoh and M. Akabori, *J. Nucl. Mater.*, 1997, **250**, 171–175.
4 K. Nakamura, T. Ogata, M. Kurata, T. Yokoo and M. A. Mignanelli, *J. Nucl. Sci. Tech.*, 2001, **38**, 112–119.
5 G. L. Hofman, L. C. Walters and T. Bauer, *Progress in Nuclear Energy*, 1997, **31**, 83–110.
6 S. Ohtsuka, T. Kaito, S. Ukai, M. Inoue, T. Okuda and A. Kimura, *J. Nucl. Mater.*, 2013, **441**, 286–292.
7 J. M. Park, H. J. Ryu, S. J. Oh, D. B. Lee, C. K. Kim, Y. S. Kim and G. Hofman, *J. Nucl. Mater.*, 2008, **374**, 422–430.
8 W. Xie, W. Xiong, C. A. Marianetti and D. Morgan, *Phys. Rev. B*, 2013, **88**, 235128.
9 D. E. Burkes, C. A. Papesch, A. P. Maddison, T. Hartmann and F. J. Rice, *J. Nucl. Mater.*, 2010, **403**, 160–166.
10 Y. S. Kim, G. Hofman and A. Yacout, *J. Nucl. Mater.*, 2009, **392**, 164–170.
11 J. L. Snelgrove, G. Hofman, M. Meyer, C. Trybus and T. Wiencek, *Nucl. Eng. Des.*, 1997, **178**, 119–126.
12 M. Farkas and Eldridge, *J. Nucl. Mater.*, 1968, **27**, 94.
13 T. Matsui, T. Natsume and K. Naito, *J. Nucl. Mater.*, 1989, **167**, 152–159.
14 T. Kutty, S. Dash, J. Banerjee, S. Kaity, A. Kumar and C. Basak, *J. Nucl. Mater.*, 2012, **420**, 193–197.
15 I. Tkach, N.-T. Kim-Ngan, A. Warren, T. Scott, A. Gonçalves and L. Havela, *Physica C*, 2014, **498**, 14–20.
16 M. D. Jones, J. C. Boettger, R. C. Albers and D. J. Singh, *Phys. Rev. B*, 2000, **61**, 4644–4650.
17 P. Söderlind, *Phys. Rev. B*, 2002, **66**, 085113.
18 B. Beeler, C. Deo, M. Baskes and M. Okuniewski, *J. Nucl. Mater.*, 2013, **433**, 143–151.
19 J. Bouchet, *Phys. Rev. B*, 2008, **77**, 024113.
20 B. Beeler, B. Good, S. Rashkeev, C. Deo, M. Baskes and M. Okuniewski, *J. Phys.: Condens. Matter*, 2010, **22**, 505703.
21 G.-Y. Huang and B. D. Wirth, *J. Phys.: Condens. Matter*, 2011, **23**, 205402.
22 G.-Y. Huang and B. Wirth, *J. Phys.: Condens. Matter*, 2012, **24**, 415404.
23 L. Fast, O. Eriksson, B. Johansson, J. M. Wills, G. Straub, H. Roeder and L. Nordström, *Phys. Rev. Lett.*, 1998, **81**, 2978–2981.
24 P. Söderlind, V. Sadigh, B.and Lordi, A. Landa and P. Turchi, *J. Nucl. Mater.*, 2014, **444**, 356–358.
25 B. Dorado, M. Freyss and G. Martin, *Eur. Phys. J. B*, 2009, **69**, 203–209.
26 A. E. Thompson, B. Meredig, M. Stan and C. Wolverton, *J. Nucl. Mater.*, 2014, **446**, 155–162.
27 D. Gryaznov, E. Heifets and E. Kotomin, *Phys. Chem. Chem. Phys.*, 2012, **14**, 4482–4490.
28 E. Bévillon, M. Ducher, R.and Barrachin and M. Dubourg, *J. Nucl. Mater.*, 2012, **426**, 189–197.
29 E. Bévillon, M. Ducher, R.and Barrachin and M. Dubourg, *J. Nucl. Mater.*, 2013, **434**, 240–247.
30 M. Klipfel, V. Di Marcello, A. Schubert, J. van de Laar and P. Van Uffelen, *J. Nucl. Mater.*, 2013, **442**, 253–261.
31 P. Alonso and G. Rubiolo, *Modelling Simul. Mater. Sci. Eng.*, 2007, **15**, 263.
32 A. Landa, P. Söderlind and P. Turchi, *J. Nucl. Mater.*, 2011, **414**, 132–137.
33 S. Jaroszewicz, E. Losada, J. Garcés and H. Mosca, *J. Nucl. Mater.*, 2013, **441**, 119–124.
34 A. R. Oganov and C. W. Glass, *J. Chem. Phys.*, 2006, **124**, 244704.
35 A. Oganov and M. Stokes, H.and Valleand, *Acc. Chem. Res.*, 2011, **44**, 227–237.
36 A. O. Lyakhov, A. R. Oganov, H. T. Stokes and Q. Zhu, *Comput. Phys. Comm.*, 2013, **184**, 1172–1182.
37 G. Kresse and J. Hafner, *Phys. Rev. B*, 1993, **47**, 558.
38 G. Kresse and J. Furthmüller, *Comput. Mater. Sci.*, 1996, **6**, 15–50.
39 G. Kresse and J. Furthmüller, *Phys. Rev. B*, 1996, **54**, 11169.
40 P. E. Blöchl, *Phys. Rev. B*, 1994, **50**, 17953.
41 G. Kresse and D. Joubert, *Phys. Rev. B*, 1999, **59**, 1758.
42 P. Hohenberg and W. Kohn, *Phys. Rev.*, 1964, **136**, B864.
43 W. Kohn and L. J. Sham, *Phys. Rev.*, 1965, **140**, A1133.
44 J. P. Perdew, K. Burke and M. Ernzerhof, *Phys. Rev. Lett.*, 1996, **77**, 3865.
45 O. Jepson and O. Anderson, *Solid State Commun.*, 1971, **9**, 1763–1767.
46 P. E. Blöchl, O. Jepsen and O. K. Andersen, *Phys. Rev. B*, 1994, **49**, 16223.
47 Y. Le Page and P. Saxe, *Phys. Rev. B*, 2002, **65**, 104104.
48 X. Wu, D. Vanderbilt and D. Hamann, *Phys. Rev. B*, 2005, **72**, 035105.
49 W. Voight, *Teubner, Leipzig*, 1928, **962**, year.
50 A. Reuss, *Z. Angew. Math. Mech*, 1929, **9**, 49–58.
51 R. Hill, *Proc. Phys. Soc. A*, 1952, **65**, 349.
52 H. J. Monkhorst and J. D. Pack, *Phys. Rev. B*, 1976, **13**, 5188.
53 J. Heyd, G. E. Scuseria and M. Ernzerhof, *J. Chem. Phys.*, 2006, **124**, 219906.
54 J. Paier, M. Marsman, K. Hummer, G. Kresse, I. C. Gerber and J. G. Ángyán, *J. Chem. Phys.*, 2006, **124**, 154709.
55 C. Franchini, R. Podloucky, J. Paier, M. Marsman and G. Kresse, *Phys. Rev. B*, 2007, **75**, 195128.
56 T. Kawakami, Y. Tsujimoto, H. Kageyama, X.-Q. Chen, C. Fu, C. Tassel, A. Kitada, S. Suto, K. Hirama, Y. Sekiya *et al.*, *Nature Chem.*, 2009, **1**, 371–376.
57 X.-Q. Chen, C. L. Fu, C. Franchini and R. Podloucky, *Phys. Rev. B*, 2009, **80**, 094527.

58 J. He, M.-X. Chen, X.-Q. Chen and C. Franchini, *Phys. Rev. B*, 2012, **85**, 195135.

59 F.-F. Wang, P.-Y. Wei, X.-Y. Ding, X.-R. Xing and X.-Q. Chen, *Chin. Phys. Lett.*, 2014, **31**, 027402.

60 T. Bučko, S. Lebègue, J. Hafner and J. G. Ángyán, *Phys. Rev. B*, 2013, **87**, 064110.

61 T. Bučko, J. Hafner, S. Lebègue and J. Ángyán, *J.Phys.Chem.A*, 2010, **114**, 11814–11824.

62 S. Grimme, J. Antony, S. Ehrlich and H. Krieg, *J.Chem.Phys.*, 2010, **132**, 154104.

63 S. Grimme, S. Ehrlich and L. Goerigk, *J.Compt.Chem.*, 2011, **32**, 1456–1465.

64 A. Togo, F. Oba and I. Tanaka, *Phys. Rev. B*, 2008, **78**, 134106.

65 A. Togo, L. Chaput, I. Tanaka and G. Hug, *Phys. Rev. B*, 2010, **81**, 174301.

66 K. Parlinski, Z. Li and Y. Kawazoe, *Phys. Rev. Lett.*, 1997, **78**, 4063.

67 A. Dwight, *J. Nucl. Mater.*, 1960, **2**, 81–87.

68 A. Wilson, *Acta Crystallogr.*, 1949, **2**, 318–321.

69 M. Alouani, R. Albers and M. Methfessel, *Phys. Rev. B*, 1991, **43**, 6500.

70 X. Chen, V. Witusiewicz, R. Podloucky, P. Rogl and F. Sommer, *Acta Mater.*, 2003, **51**, 1239–1247.

71 M. Methfessel and A. Paxton, *Phys. Rev. B*, 1989, **40**, 3616.

72 Z.-J. Wu, E.-J. Zhao, H.-P. Xiang, X.-F. Hao, X.-J. Liu and J. Meng, *Phys. Rev. B*, 2007, **76**, 054115.

73 A. A. Luo, B. R. Powell and M. P. Balogh, *Metall. Mater. Trans. A*, 2002, **33**, 567–574.

Table 1 The optimized structural parameters (lattice constant in Å , the atomic positions) and enthalpy of formation (ΔH_f in eV/atom) for both *I*4/*mmm* and *Pmmn* phases of U_2Mo within standard DFT and DFT+D, as compared with available experimental data.

	a	b	c	ΔH_f	U	Mo	
$Im\bar{3}m$-U	3.433	3.433	3.433	-	(0,0,0)	-	DFT
$Im\bar{3}m$-U	3.372	3.372	3.372	-	(0,0,0)	-	DFT+D
$Im\bar{3}m$-U	3.47	3.47	3.47	-	(0,0,0)	-	Expt[68]
$Im\bar{3}m$-Mo	3.149	3.149	3.149	-	-	(0,0,0)	DFT
$Im\bar{3}m$-Mo	3.120	3.120	3.120	-	-	(0,0,0)	DFT+D
$Im\bar{3}m$-Mo	3.148	3.148	3.148	-	-	(0,0,0)	Expt[69]
Pmmn	4.831	8.315	2.720	-0.145	(0,0.167,1.0)	(0,0.5,0.5)	DFT
Pmmn	4.765	8.252	2.682	-0.161	(0,0.167,1.0)	(0,0.5,0.5)	DFT+D
*I*4/*mmm*	3.417	3.417	9.714	-0.103	(0,0,0.321)	(0,0,0)	DFT
*I*4/*mmm*	3.379	3.379	9.590	-0.090	(0,0,0.321)	(0,0,0)	DFT+D
*I*4/*mmm*	3.440	3.440	9.631	-	(0,0,0.321)	(0,0,0)	Calc[33]
*I*4/*mmm*	3.427	3.427	9.834	-	(0,0,0.328)	(0,0,0)	Expt[67]
*I*4/*mmm*	-	-	-	-0.064	-	-	Calc[31]
*I*4/*mmm*	-	-	-	-0.034	-	-	Calc[32]

Table 2 Calculated elastic constants(in GPa), Possion's ratio (ν), sound velocity (V_l, V_t and V_m in m/s), Debye Temperature (Θ_D in K), theoretical density (ρ in g/cm^3) at 0 K within standard DFT and DFT+D. BC and MP represent Blöchl corrections method and Methfessel-Paxton method for how the partial occupancies were set for each orbital, respectively.

	C11	C12	C13	C33	C44	C66	C22	C23	ρ	Note
*I*4/*mmm*	254	161	125	295	38	∼20	-	-	-	BC, Calc[33]
*I*4/*mmm*	255	165	124	302	37	-12	-	-	16.75	BC
*I*4/*mmm*	287	121	123	314	8	9	-	-	16.75	MP
*I*4/*mmm*	272	186	137	333	46	-12	-	-	17.35	DFT+D
Pmmn	299	131	116	246	74	87	293	133	17.26	BC
Pmmn	270	122	109	219	75	83	282	123	17.26	MP
Pmmn	361	133	118	327	70	108	352	122	18.02	DFT+D
	C55	B	E	G	ν	V_l	V_t	V_m	Θ_D	Note
*I*4/*mmm*	-	180	102	36	0.4		-	-	-	BC, Calc[33]
*I*4/*mmm*	-	182	-	-	-	-	-	-	-	BC
*I*4/*mmm*	-	180	74	26	0.4	3582	1258	1411	195	MP
*I*4/*mmm*	-	200	-	-	-	-	-	-	-	DFT+D
Pmmn	73	176	202	77	0.31	4020	2114	2346	265	BC
Pmmn	77	161	194	75	0.30	3892	2080	2306	261	MP
Pmmn	69	198	238	91	0.30	4214	2252	2497	286	DFT+D

Table 3 Calculated elastic constants(in GPa) and Debye Temperature (Θ_D in K) of *Pmmn* U_2Mo as a function of temperature (in K) within standard DFT.

Temperature	C11	C22	C33	C44	C55	C66	C12	C13	C23	Θ_D
0	299	293	246	74	73	87	131	116	133	265
100	295	288	230	73	72	85	131	112	125	266
200	290	284	226	72	71	84	129	110	123	261
300	285	281	221	72	71	83	128	109	122	259
450	278	268	214	71	69	81	124	107	117	256
880	258	254	192	69	66	76	118	100	107	249